

# Detecting Protein-Ligand Interactions with Nitroxide Based Paramagnetic Cosolutes

Anja Penk,<sup>[a]</sup> Annemarie Danielsson,<sup>[b]</sup> Margrethe Gaardløs,<sup>[b]</sup> Cindy Montag,<sup>[a]</sup> Andrea Schöler,<sup>[c]</sup> Daniel Huster,<sup>[a]</sup> Sergey A. Samsonov,<sup>\*[b]</sup> and Georg Künze<sup>\*[c]</sup>

NMR spectroscopy techniques can provide important information about protein-ligand interactions. Here we tested an NMR approach which relies on the measurement of paramagnetic relaxation enhancements (PREs) arising from analogous cationic, anionic or neutral soluble nitroxide molecules, which distribute around the protein-ligand complex depending on near-surface electrostatic potentials. We applied this approach to two protein-ligand systems, interleukin-8 interacting with highly charged glycosaminoglycans and the SH2 domain of Grb2 interacting with less charged phospho-tyrosine tripeptides.

The electrostatic potential around interleukin-8 and its changes upon binding of glycosaminoglycans could be derived from the PRE data and confirmed by theoretical predictions from Poisson-Boltzmann calculations. The ligand influence on the PREs and NMR-derived electrostatic potentials of Grb2 SH2 was localized to a narrow protein region which allowed the localization of the peptide binding pocket. Our analysis suggests that experiments with nitroxide cosolutes can be useful for investigating protein-ligand electrostatic interactions and mapping ligand binding sites.

## Introduction

Elucidating the binding mode of biological macromolecules with their ligands is essential for understanding the biological effects triggered by the ligand binding process as well as for the discovery and design of new bioactive molecules. Nuclear magnetic resonance (NMR) spectroscopy represents a versatile approach to characterize protein-ligand interactions and is sensitive to a wide range of ligand affinities (nanomolar to millimolar).<sup>[1]</sup> Several NMR methods are available to obtain structural, thermodynamic, and kinetic information about protein-ligand systems.<sup>[2]</sup> For example, the measurement of chemical shift perturbations (CSPs) allows calculation of equilibrium dissociation constants and identification of protein residues that bind the ligand. An advantage of the CSP method is its ability to capture protein conformational changes, which

can occur upon ligand binding. This provides opportunities for identifying and targeting allosteric binding sites.<sup>[3,4]</sup> However, care must be taken in the interpretation of CSPs since they can reflect either direct protein-ligand interactions or secondary conformational effects. Other NMR methods, such as saturation transfer difference (STD) NMR spectroscopy,<sup>[5]</sup> transferred nuclear Overhauser effect (NOE) NMR spectroscopy,<sup>[6]</sup> and the Water-LOGSY method,<sup>[7]</sup> rely on detecting the NMR signals of the ligand. STD NMR and Water-LOGSY can be used to determine the ligand moieties that are important for binding<sup>[8]</sup> and also to screen mixtures of ligand fragments for their ability to bind to proteins.<sup>[9,10]</sup> Transferred NOEs can be utilized to determine the ligand conformation in the bound state,<sup>[11]</sup> which can be helpful for modeling the 3D structure of the protein-ligand complex. Moreover, they can be used for ligand screening.<sup>[12]</sup>

Paramagnetic NMR methods further expand the application range of NMR in drug research.<sup>[13]</sup> An important application of paramagnetic NMR is the collection of structural restraints on the ligand binding pose which can guide the drug design process in medicinal chemistry. This is especially useful in the early stages of drug discovery when crystal structures of weakly binding ligands are difficult to obtain. The paramagnetic restraints such as pseudocontact shifts (PCSs) or paramagnetic relaxation enhancements (PREs) can be integrated via different approaches to guide ligand docking calculations or filter the generated interaction models. PCSs can be used in a similar manner as CSPs to locate the ligand binding site. In order to exploit the paramagnetic effects, different approaches for attaching the paramagnetic center (e.g. a nitroxide radical or lanthanide ion) to the receptor protein or ligand molecule of interest exist.<sup>[14–22]</sup> While the PCS approach is well suited for fast-exchanging ligands with micro- to millimolar dissociation constants, PCSs on tightly binding, slow-exchanging ligands

[a] Dr. A. Penk,<sup>+</sup> C. Montag, Prof. Dr. D. Huster

Institute for Medical Physics and Biophysics  
University of Leipzig  
Härtelstr. 16/18, D-04107 Leipzig, Germany

[b] A. Danielsson,<sup>\*</sup> Dr. M. Gaardløs, Prof. Dr. S. A. Samsonov

Faculty of Chemistry  
University of Gdańsk  
Ul. Wita Stwosza 63, 80-308 Gdańsk, Poland  
E-mail: sergey.samsonov@ug.edu.pl

[c] A. Schöler, Dr. G. Künze

Institute for Drug Discovery  
University of Leipzig  
Brüderstr. 34, D-04103 Leipzig, Germany  
E-mail: georg.kuenze@uni-leipzig.de

 Supporting information for this article is available on the WWW under <https://doi.org/10.1002/chem.202303570>

 © 2023 The Authors. Chemistry - A European Journal published by Wiley-VCH GmbH. This is an open access article under the terms of the Creative Commons Attribution Non-Commercial License, which permits use, distribution and reproduction in any medium, provided the original work is properly cited and is not used for commercial purposes.

could be detected using special reporter groups e.g. tert-butyl<sup>[18]</sup> or <sup>19</sup>F nuclei.<sup>[19]</sup>

One concern about these covalent tagging approaches is that the addition of such large tags to the ligand molecule could significantly alter its binding mode. Affinity data are also not easily transferrable to the untagged ligand. Thus, tagging-free NMR techniques represent an interesting alternative. Solvent PRE (sPRE) effects can be induced by soluble, paramagnetic probes that are directly added to the protein solution, requiring no chemical modification of the protein or ligand. sPREs offer a rich source of structural information and have been used for a variety of applications in structural biology, e.g., for the mapping of the solvent accessible surface of biomolecules,<sup>[23,24]</sup> protein structure prediction,<sup>[25,26]</sup> the detection of transient conformational states,<sup>[27]</sup> and the localization of the binding interface in protein-protein complexes.<sup>[28–30]</sup> Recently, Iwahara and coworkers developed an NMR method that uses paramagnetic 2,2,5,5-tetramethylpyrrolidine-N-oxyl nitroxide (PROXYL) cosolutes to determine the local electrostatic potential ( $\phi$ ) around biomolecules.<sup>[31–33]</sup> Specifically, two oppositely charged PROXYL molecules are used and their PRE effects are quantified. The PROXYL probes distribute around the macromolecule according to the near-surface electrostatic potential ( $\phi_{ENS}$ ), which can be determined with per-residue resolution from the ratio of PRE rates induced by the two PROXYL derivatives. The authors concluded, that the NMR-derived data of  $\phi_{ENS}$  agreed well with predictions from the Poisson-Boltzmann theory and that this method could be used for the *de novo* determination of  $\phi_{ENS}$ .<sup>[31]</sup>

Electrostatic interactions play an important role in protein-ligand recognition processes.<sup>[34]</sup> They account for a sizeable contribution to the binding affinity and the stabilization of weakly specific transition states that occur along the binding pathway.<sup>[35]</sup> Furthermore, electrostatic complementarity at the protein-ligand interface is recognized as an important factor for predicting and optimizing ligand affinity and selectivity.<sup>[36,37]</sup> We reasoned that the ionic PROXYL probes could also be useful for the detection of protein-ligand interactions, in particular for ligands bearing charged chemical groups, since those will significantly perturb the protein electrostatic potential in the binding site. Here, we extend the PROXYL method to the investigation of protein-ligand complexes and apply it to two protein-ligand systems, the protein interleukin-8 (IL-8), interacting with glycosaminoglycans (GAGs), and the src-homology 2 (SH2) domain of the growth factor receptor-bound protein 2 (Grb2), interacting with phosphotyrosine peptides.

IL-8 is, depending on its splicing variant, a 8–9 kDa protein that belongs to the CXC chemokine family and plays important roles in the activation and recruitment of neutrophil granulocytes to sites of inflammation.<sup>[38,39]</sup> IL-8 strongly interacts with GAGs from the extracellular matrix, such as heparan sulfate or chondroitin sulfate. The interaction with GAGs contributes to the formation of a dynamic chemokine gradient which mediates the attraction and migration of immune cells.<sup>[40]</sup> GAGs are highly negatively charged polysaccharides consisting of periodic disaccharide units and carry a large number of sulfate groups. Heparin (HP) is the most highly sulfated member of the

GAG family and an important pharmaceutical anticoagulant. The interaction of IL-8 with HP and other GAGs has been demonstrated by several experimental and computational studies which revealed important GAG binding residues on IL-8 as well as the binding mode for shorter GAG fragments.<sup>[41–47]</sup>

Grb2 is a 25 kDa adaptor protein consisting of one SH2 domain and two SH3 domains, arranged in the order SH3-SH2-SH3.<sup>[48]</sup> The SH2 domain is a small domain of approximately 100 amino acid residues which binds to specific tyrosine phosphorylation sites on several proteins.<sup>[49]</sup> Binding of the Grb2 SH2 domain to phosphotyrosine (pY) motifs on receptors, e.g. EGF receptor,<sup>[50]</sup> recruits the Ras exchange factor Sos at the plasma membrane where Sos stimulates nucleotide exchange on Ras, triggering the downstream signaling of Raf and MAP kinases.<sup>[51]</sup> The phosphotyrosine (pY) recognition consensus sequence of Grb2 SH2 is pYXN, where X represents any amino acid and N represents asparagine.<sup>[52,53]</sup>

In this study, we evaluate the applicability of the PROXYL method for mapping ligand binding sites in IL-8 and Grb2 SH2, and for detecting changes in the protein near-surface electrostatic potential ( $\phi_{ENS}$ ) induced by interactions with their respective ligands. Our results show that the PROXYL method can detect ligand-induced changes of  $\phi_{ENS}$ , which are in good agreement with theoretical predictions. A highly charged HP ligand alters the PRE and  $\phi_{ENS}$  data across a large region in IL-8, while pYXN peptides cause more localized changes in a narrow region in Grb2 SH2, which allow a precise localization of the peptide binding site. Our findings suggest that experiments with paramagnetic cosolutes can be a useful addition to the toolbox of NMR methods for studying protein-ligand interactions.

## Results and Discussion

### Calculation of the electrostatic potential of IL-8

The soluble PROXYL probes distribute around the protein according to its electrostatic potential. We first investigated the strength and distribution of  $\phi_{ENS}$  of IL-8 using computational approaches. Starting from the homodimeric NMR structure of IL-8<sup>[54]</sup> we sampled an ensemble of structures of IL-8 using molecular dynamics (MD) simulation and calculated  $\phi_{ENS}$  for these structures using the Adaptive Poisson-Boltzmann Solver (APBS) software.<sup>[55,56]</sup> Figure 1A shows mappings of  $\phi_{ENS}$  for different isosurface values. As can be seen in Figure 1A,  $\phi_{ENS}$  is mostly positive over large regions around IL-8 since IL-8 is strongly positively charged at neutral pH.

We then applied molecular docking and MD simulation to model the complex of IL-8 with GAGs and studied the influence of GAG binding on  $\phi_{ENS}$ . We chose two different GAGs, HP and hyaluronan (HA), because of their different charge densities. While HP contains a maximum of four negatively charged groups per disaccharide, HA features only one negatively charged carboxyl group per disaccharide and is the GAG with the lowest net charge. For computational efficiency, both GAGs were modeled as hexasaccharides (dp6, where dp stands for

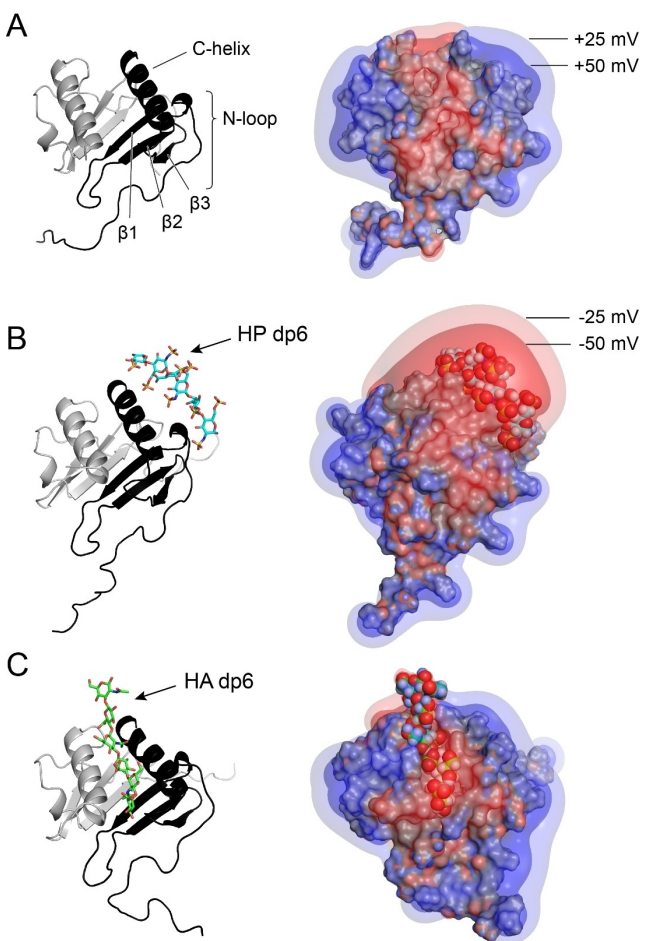


**Figure 1.** Simulated electrostatic potentials for IL-8 and IL-8-ligand complexes. (A) IL-8 apo. Secondary structure regions are labeled. (B) IL-8/HP dp6 complex. (C) IL-8/HA dp6 complex.

degree of polymerization). The binding pose of HP dp6 with the lowest energy in the MD simulation is displayed in Fig 1B. The HP dp6 molecule adopts an extended conformation located between the C-helix and N-loop of one IL-8 monomer and oriented parallel to the C-terminal C-helix. This binding pose corresponds to the one previously analyzed by us and others, both theoretically and experimentally.<sup>[44,46,47,57,58]</sup> The lowest energy binding pose of HA dp6 observed in the MD simulations was located in a central groove formed by the two C-helices of the IL-8 dimer (Figure 1C). This alternative GAG binding pose is not unexpected. It was observed in previous simulation studies,<sup>[44,47,58]</sup> however, was less populated than the binding pose between N-loop and C-helix. It was also seen in some MD runs with HP dp6 in this study. As expected from the high negative charge of HP dp6 of  $-12e$ , it strongly changes  $\phi_{ENS}$  around IL-8 to more negative (Figure 1B). By contrast, HA dp6 has a comparatively small effect and does not significantly change  $\phi_{ENS}$  in the environment of IL-8 (Figure 1C).

## Paramagnetic NMR data for IL-8 and IL-8/GAG complexes

Next, the distribution of  $\phi_{ENS}$  around IL-8 and IL-8/GAG complexes was investigated experimentally using paramagnetic NMR. We used  $^{15}\text{N}$ -labeled IL-8 and prepared the protein as previously described yielding the homodimeric form of IL-8(1–77) in the used NMR concentrations.<sup>[44]</sup> We used the paramagnetic PROXYL derivatives shown in Figure 2A as cosolutes and measured the  $^1\text{H}$  transverse PRE rates ( $\Gamma_2$ ) for the  $^1\text{H}_\text{N}$  backbone amide groups of IL-8 (example spectrum of IL-8 in Fig S1) using the two time-point approach (see Experimental Section). Specifically, cationic aminomethyl-PROXYL and anionic carboxy-PROXYL were used to measure  $\Gamma_{2,+}$  and  $\Gamma_{2,-}$  rates, respectively. We observed clear signal intensity changes for many resonances in the  $^1\text{H}-^{15}\text{N}$  HSQC spectrum of IL-8 (examples shown in Fig 2B) relative to the diamagnetic reference spectrum. This allowed us to measure  $\Gamma_{2,+}$  rates for 55 residues and  $\Gamma_{2,-}$  rates for 58 residues in IL-8, respectively (Table S1). As can be seen from the signal slices in Fig 2B and the PRE-vs-residue number plot in Fig 2C, the  $\Gamma_{2,+}$  and  $\Gamma_{2,-}$  rates vary significantly for several residues of IL-8. Large  $\Gamma_{2,+}$  rates above 40 Hz were measured for residues in the N-terminus, the N-loop, and the  $\beta_2$  and  $\beta_3$  strand. Large  $\Gamma_{2,-}$  rates above 40 Hz were observed for residues in the N-loop, the  $\beta_3$  strand and the C-helix (Fig 2C). The different patterns of  $\Gamma_{2,+}$  versus  $\Gamma_{2,-}$  rates are also evident from their mapping onto the 3-dimensional structure of IL-8 shown in Fig S2. This indicates that the two oppositely charged PROXYL molecules distribute with a different probability density in the electric field generated by IL-8.

Next, we prepared samples of IL-8 with HP dp6 or HA dp6, respectively, by stepwise titration with GAG, while recording a  $^1\text{H}-^{15}\text{N}$  HSQC spectrum for each titration step (see Fig S3 and S4). As expected from previous NMR studies,<sup>[44]</sup> some protein precipitation was observed during the titration of HP, which indicated a strong interaction with GAG. To avoid that the protein was completely precipitated, a concentration not higher than an equimolar ratio of IL-8 and HP had to be used. We monitored the interaction of HP with IL-8 by measuring CSPs from  $^1\text{H}-^{15}\text{N}$  HSQC spectra and mapped the CSPs to the IL-8 amino acid sequence (Fig S4A). In line with our previous NMR studies,<sup>[44]</sup> the largest CSPs above a threshold of 0.02 ppm were found for residues in the N-loop (K20, H23, K25, K28) and the C-helix (K59, W62, V63, Q64, V66, V67, E68, K69, F70, A74, E75). This set of residues matches the modeled binding pose of HP dp6 that was observed in the MD simulation (Fig 1B), showing that most interactions of HP dp6 are formed with the N-loop and C-helix of IL-8.

Compared to HP dp6, the CSPs induced by HA dp6 were considerably smaller ( $< 0.01$  ppm) (Fig S4B), indicating that it binds weakly to IL-8.<sup>[44]</sup> However, a similar CSP pattern was observed, with the highest changes found for residues in the  $\beta_1$  strand (K28) and the end of the C-helix (A74, E75).

We next monitored the interaction of IL-8 with HP dp6 and HA dp6 using aminomethyl-PROXYL and carboxy-PROXYL probes, respectively, and compared the PRE rates of IL-8 measured in the presence and absence of GAG. The PROXYL-induced signal intensity changes relative to the diamagnetic

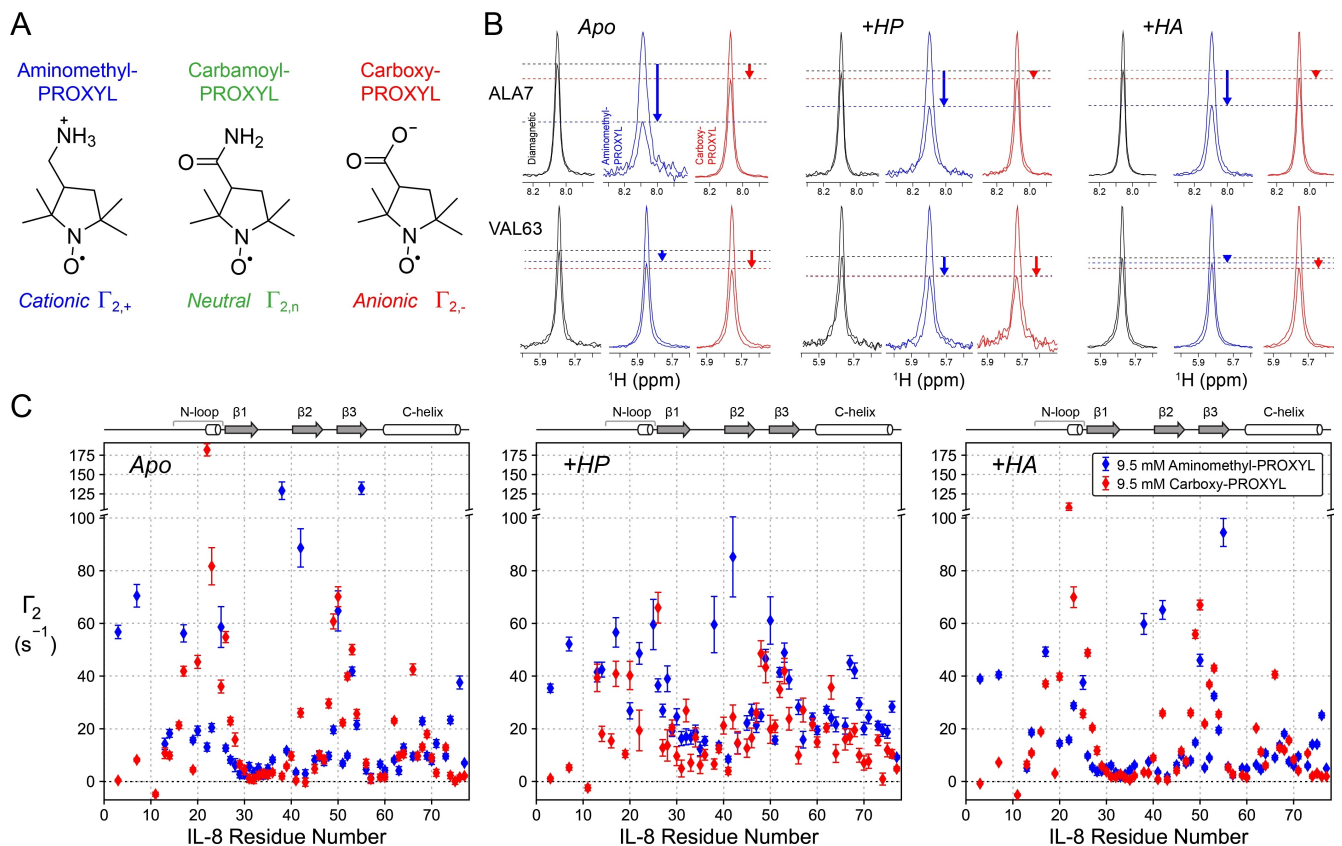


**Figure 2.** Paramagnetic NMR data used to analyze the electrostatic potentials around IL-8 and IL-8/GAG complexes. (A) Paramagnetic cosolute molecules used in this study. (B) Examples of signal intensity changes used to measure  $^1\text{H}_\text{N}$  PRE rates of IL-8 apo protein and IL-8 in the presence of HP dp6 or HA dp6, respectively. The  $^1\text{H}$  slices of the  $^1\text{H}_\text{N}$  signals of A7 and V63 from the HSQC spectra of IL-8 at 0 ms and 10 ms relaxation measurement delays are shown. The  $^1\text{H}$  signal slices in the absence (diamagnetic) or presence of 9.5 mM paramagnetic PROXYL derivative normalized to the intensity at 0 ms are displayed. Signal change differences observed in the presence of aminomethyl-PROXYL or carboxy-PROXYL compared to the diamagnetic case are indicated with blue or red arrows, respectively. (C) The PRE rates  $\Gamma_{2,+}$  (blue) and  $\Gamma_{2,-}$  (red) measured for the backbone  $^1\text{H}_\text{N}$  nuclei in IL-8 in the absence and presence of HP dp6 or HA dp6, respectively, are plotted versus the IL-8 residue number. Error bars represent the  $\Gamma_2$  rate uncertainties (see Experimental Section). The  $^1\text{H}_\text{N}$  PRE rates of IL-8 are summarized in Table S1 in the supporting material.

reference were clearly different for several IL-8 residues upon addition of HP and HA. This is exemplarily shown for the NMR signals of A7 and V63 in Fig 2B. Figure 2C displays the  $\Gamma_{2,+}$  and  $\Gamma_{2,-}$  rates along the IL-8 residue number for the cases without GAG, with HP, and with HA, respectively (see also Table S1). Comparing the GAG-free and HP-bound PRE datasets, the  $\Gamma_{2,+}$  rates are clearly increased in the presence of HP for almost all residues in IL-8, as can be seen in Figure 2C and supporting Fig S5A. The  $\Gamma_{2,-}$  rates on the other hand are less strongly increased by HP compared to the  $\Gamma_{2,+}$  rates (Fig S5A). This result indicates that cationic aminomethyl-PROXYL molecules become more enriched around the IL-8/HP complex and that HP binding to IL-8 renders  $\phi_{\text{ENS}}$  more negative as suggested by the APBS calculations (Figure 1B). Furthermore, the  $\Gamma_{2,+}$  rates are most strongly increased for residues in the N-loop,  $\beta$ 1 strand, and C-helix (Fig S5A), which is in line with the computationally predicted binding sites for HP dp6 (Figure 1B).

The PRE datasets for IL-8 and IL-8/HA are overall more similar. The  $\Gamma_{2,+}$  and  $\Gamma_{2,-}$  rates are not increased in the presence of HA, but are even slightly decreased (Fig S5A). This indicates that HA binding has only a small influence on the distribution of PROXYL molecules around IL-8 and consequently on  $\phi_{\text{ENS}}$ .

This can also be seen when comparing the computationally predicted  $\phi_{\text{ENS}}$  isosurfaces for IL-8 apo and IL-8/HA in Figure 1.

Interestingly, the PREs of a few isolated residues are largely decreased in the presence of both HP and HA. The  $\Gamma_{2,+}$  rate of H38 and the  $\Gamma_{2,-}$  rate of F22 are over 100 Hz in the absence of GAG and are reduced by more than 60 Hz upon addition of HP or HA (Fig S5). Similarly, the  $\Gamma_{2,+}$  rates of L3, A7 and C55 are reduced by 20–30 Hz in the presence of HP and HA. A possible explanation could be that those residues in IL-8 undergo direct interactions with the PROXYL molecules, leading to their fast relaxation, and that HP and HA binding blocks those direct IL-8-PROXYL interactions, reducing the strong PRE effects.

In summary, we conclude based on the observed PRE changes that GAGs, in particular HP, profoundly affect the interaction of IL-8 with PROXYL molecules. In accordance with our APBS calculations, this supports the notion that HP renders  $\phi_{\text{ENS}}$  more negative while HA has a comparatively small influence on  $\phi_{\text{ENS}}$ .

### NMR-determined near-surface electrostatic potentials for IL-8 and IL-8/GAG complexes

In order to more quantitatively analyze the effect of GAGs on the electrostatic potential of IL-8, we determined  $\phi_{ENS}$  for IL-8 and IL-8/GAG complexes using the measured  $\Gamma_{2,+}$  and  $\Gamma_{2,-}$  rates (Figure 2C, Table S1) and applying equation 1 (see Experimental Section). We only considered statistically significant PRE rates and  $\Gamma_{2,+}/\Gamma_{2,-}$  ratios (see Experimental Section). This procedure yielded  $\phi_{ENS}$  values for 38 residues of IL-8, 41 residues of IL-8/HP dp6, and 41 residues of IL-8/HA dp6, respectively. Fig 3A shows  $\phi_{ENS}$  values (black) for individual residues in IL-8 in the GAG-free case, and in the presence of either HP dp6 or HA dp6, respectively. For comparison with the experimental  $\phi_{ENS}$  values, we calculated theoretical  $\phi_{ENS}$  potentials using the APBS software<sup>[55,56]</sup> and structural models of IL-8 or IL-8/GAG complexes generated by docking and subsequent MD simulation. From the APBS-computed potential at each grid point in the exterior of the protein structure, we calculated the theoretical  $\phi_{ENS}$  potential of each  $^1\text{H}_\text{N}$  nucleus of IL-8 by applying equations 1 and 2 (see Experimental section). The accessibility of each grid point was assessed by measuring the distance to the closest protein or GAG atom and comparing it to the sum of the van der Waals radius of the biomolecular atom and the accessibility radius of the paramagnetic PROXYL probe of 3.5 Å (Experimental Section). The theoretical  $\phi_{ENS}$  profile plotted in Figure 3A (red) shows the average  $\pm$  S.D. of  $\phi_{ENS}$  over a 100 ns MD simulation. Overall, the experimental  $\phi_{ENS}$  data agreed well with the simulated data, in particular for residues in secondary

structure regions. Correlation plots of experimental versus simulated  $\phi_{ENS}$  values for IL-8, IL-8/HP, and IL-8/HA are shown in Fig 3B. The RMSD between experimental and simulated  $\phi_{ENS}$  values in the structured regions was 10.1 mV (IL-8), 10.5 mV (IL-8/HP), and 9.5 mV (IL-8/HA). The correlation coefficients for secondary structure regions were 0.57 (IL-8), 0.40 (IL-8/HP), and 0.49 (IL-8/HA). The largest outliers were observed for residues in loop regions, e.g., for L3 and A7 in the N-terminus, H38 in the  $\beta_1$ - $\beta_2$  loop, and N76 in the C-terminus. The discrepancy between experimental and simulated  $\phi_{ENS}$  data for the residues in loop regions is most likely due to increased conformational flexibility of those parts of the IL-8 structure. This is supported by the observations of Yu et al.<sup>[31]</sup> who found in their paramagnetic NMR study on ubiquitin the largest outliers in loop regions. The authors attributed the discrepancy to increased conformational heterogeneity, which poses a challenge to structure-based electrostatic potential prediction. We also calculated the standard deviation of the predicted  $\phi_{ENS}$  data using 100 structures equally sampled from the 100 ns MD simulation for each IL-8 or IL-8/GAG system. The standard deviation was highest in the N-terminus, the  $\beta_1$ - $\beta_2$  loop, and the  $\beta_3$  strand (Figure 3A), which are regions of increased flexibility. This supports the notion that considering protein flexibility is critical for the prediction of the electrostatic potential. Improving the conformational sampling of the protein structure, e.g., by extending the time length of the MD simulation, could therefore potentially improve the agreement of the  $\phi_{ENS}$  data with the experiment.

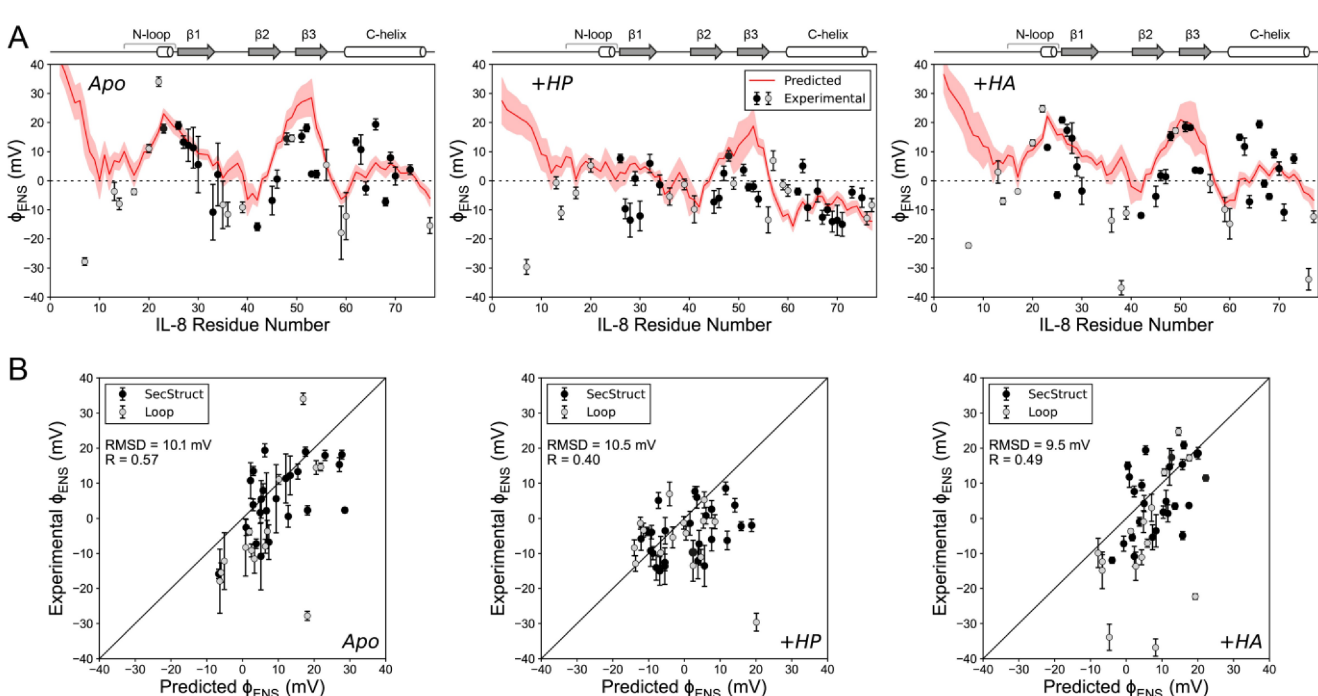


**Figure 3.** ENS electrostatic potentials ( $\phi_{ENS}$ ) determined from the  $^1\text{H}_\text{N}$  PRE NMR data of IL-8 and IL-8/GAG complexes. (A) Experimentally determined (black and gray points) and predicted  $\phi_{ENS}$  data (red line) for IL-8 apo (left), IL-8/HP (middle), and IL-8/HA (right) plotted along the residue number for IL-8. The predicted  $\phi_{ENS}$  values represent the mean of the ENS potentials calculated from a 100 ns MD simulation of IL-8 or IL-8/GAG complexes. The red shaded region indicates the standard deviation of the  $\phi_{ENS}$  predictions. Data points for residues located in secondary structure regions are shown in black and those for residues in loop regions are colored gray. (B) Correlation between experimental and predicted  $\phi_{ENS}$  data. Error bars represent the experimental  $\phi_{ENS}$  value uncertainties (see Experimental Section).

Comparing the  $\phi_{ENS}$  data of IL-8 with those of IL-8/HP and IL-8/HA, some distinct differences can be noticed. The presence of HP leads to a reduction of  $\phi_{ENS}$  across large parts of IL-8. The reduction is most significant in the N-loop,  $\beta$ 1 strand,  $\beta$ 3 strand, and the C-helix (middle plot in Fig 3A). This can be explained by the highly negatively charged character of HP dp6 ( $q = -12e$ ) and by the fact that HP dp6 binds close to those regions in the IL-8 structure. As seen in Fig 1B, HP dp6 gives rise to an extensive area of negative potential around IL-8. This is in contrast to the IL-8/HA dp6 complex, which is displayed in Figure 1C. The  $\phi_{ENS}$  profile (right plot in Figure 3A) is not significantly different from that of apo IL-8, and the spatial distribution of  $\phi_{ENS}$  is not significantly perturbed. This is consistent with the small negative charge of HA dp6 of  $-3e$ .

In conclusion, while the interaction of IL-8 with HP dp6 can be clearly detected from the changes of  $\phi_{ENS}$  using paramagnetic NMR, the interaction with HA dp6 cannot be deduced based on experimental  $\phi_{ENS}$  measurements. This could indicate that the PROXYL method is more suitable for the detection of highly charged ligand interactions. In addition, we observed that the HP-induced  $\phi_{ENS}$  changes around IL-8 were not limited to only a handful of amino acid residues, but occurred over multiple regions of the protein. This could be due to the high charge and large size of the HP dp6 molecule. While this effect could be helpful for the detection of biomolecular interactions, it also limits the site-selectivity of the structural information. Furthermore, while HP has the highest negative charge density of any known biological molecule, many small drug molecules are less strongly charged, which could imply possible limitations of the approach. It is an interesting question if drug interactions with proteins can also be studied with paramagnetic PROXYL probes. Thus, to further explore the capabilities and limitations of paramagnetic PROXYL probes for detecting protein-ligand interactions, we decided to test this approach on another group of ligands that were smaller and less strongly charged as HP.

## Calculation of the electrostatic potential around Grb2 SH2 and Grb2 SH2/peptide complexes

As an additional test system we used the SH2 domain of Grb2 which recognizes phosphotyrosine peptides containing a pYXN recognition motif (where X can be any residue).<sup>[52,53]</sup> Grb2 SH2 was prepared by expression in *E. coli* with a C-terminal His<sub>6</sub> tag for purification purposes (see Experimental Procedures). We tested three different small pYXN tripeptides, which carried in their middle position either a neutral (valine, V), positively charged (lysine, K), or negatively charged amino acid (glutamic acid, E). At physiological pH (7.4), these peptides have a net charge of ca.  $-2e$  (pYVN),  $-1e$  (pYKN), or  $-3e$  (pYEN), respectively. The N- and C-termini were capped with acetyl and amide groups, respectively, to avoid any unspecific interactions due to the free termini. Based on the crystal structure of Grb2 SH2 bound to a longer PSpYVNQN peptide (PDB: 1JYR<sup>[59]</sup>), we modeled the complex of Grb2 SH2 with each pYXN tripeptide using docking and MD simulation. Representative structural models from the MD simulation are displayed in Figure 4. Using the APBS software,<sup>[55,56]</sup> we calculated  $\phi_{ENS}$  for each Grb2 SH2/peptide complex and apo Grb2 SH2, which is mapped on the protein surface shown in Figure 4.

All pYXN peptides share a common binding mode. The phosphotyrosine side chain binds to a region with high positive  $\phi_{ENS}$  formed by the side chains of R67 ( $\alpha$ 1 helix), R86 ( $\beta$ 1 strand), S88 ( $\beta$ 1 strand), K109 ( $\beta$ 3 strand), and the backbone HN of E89 ( $\beta$ 1- $\beta$ 2 loop). The asparagine side chain of pYXN is hydrogen-bonded to the backbone of K109 ( $\beta$ 3 strand) and capped by the side chain of Trp121 ( $\beta$ 3- $\alpha$ 2 loop) of Grb2 SH2. The middle residue X binds to a small pocket formed by Q106 ( $\beta$ 3 strand), F108 ( $\beta$ 3 strand), S141, and N143 (both in the loop after  $\alpha$ 2).

As can be seen in Fig 4, Grb2 SH2 exhibits an extended region of positive  $\phi_{ENS}$  which is formed by several cationic residues (R67 ( $\alpha$ 1 helix), R86 ( $\beta$ 1 strand), K109 ( $\beta$ 3 strand)). This

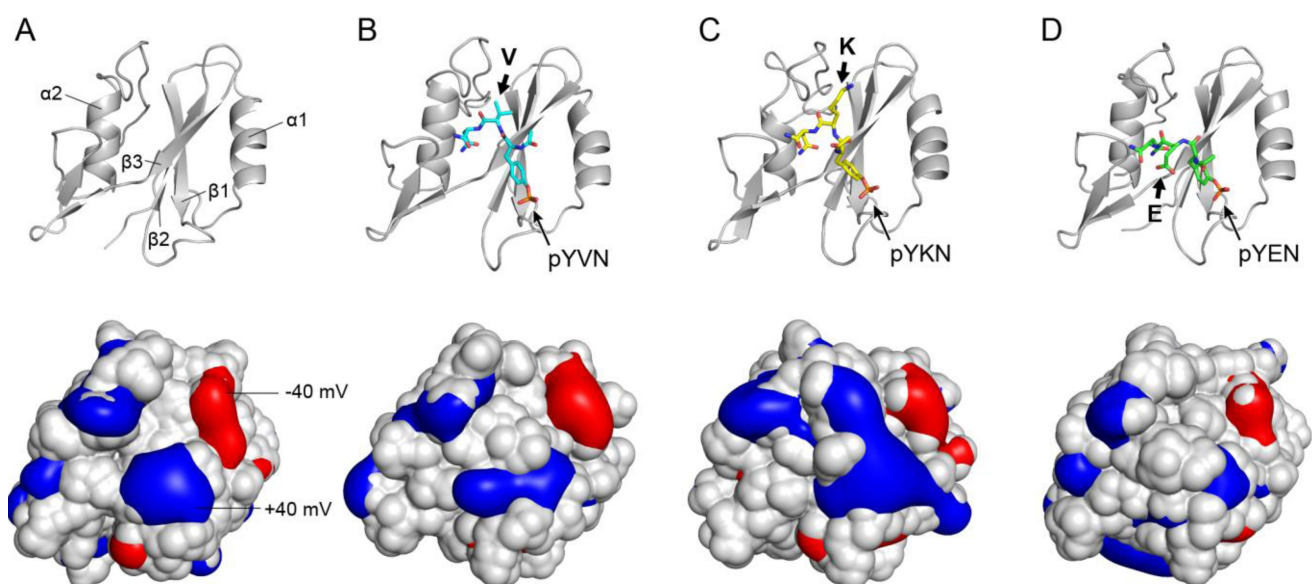


**Figure 4.** Simulated electrostatic potentials for Grb2 SH2 apo and Grb2 SH2/peptide complexes. (A) Grb2 SH2 apo. Secondary structure regions are labeled. (B) Grb2 SH2 with pYVN ( $q = -2e$ ). (C) Grb2 SH2 with pYKN ( $q = -1e$ ). (D) Grb2 SH2 with pYEN ( $q = -3e$ ).

positive pocket binds the phosphotyrosine group of the pYXN peptides and is one of the structural determinants for the recognition of phospho-tyrosine peptides by Grb2 SH2. Another smaller region of negative  $\phi_{ENS}$  is formed by the side chains of E71, E72 (both  $\alpha$ 1 helix), and D104 ( $\beta$ 3 strand), but is not part of the peptide binding pocket. The binding of pYVN and pYEN reduces slightly the size of the positive  $\phi_{ENS}$  region (Figure 4B and D) and the binding of pYKN slightly increases its size, while the negative  $\phi_{ENS}$  region is not significantly changed by any of the tripeptides. To monitor the interaction of pYXN peptides with Grb2 SH2 by NMR and experimentally measure  $\phi_{ENS}$  around the protein as well as the ligand induced changes of  $\phi_{ENS}$ , we next conducted NMR experiments with paramagnetic PROXYL probes.

### Paramagnetic NMR data on Grb2 SH2 and Grb2 SH2/peptide complexes

We used  $^{15}\text{N}$ -labeled Grb2 SH2 and unlabeled pYXN peptides. The resonance assignment of the  $^1\text{H}-^{15}\text{N}$  HSQC spectrum of Grb2 SH2 (see Fig S6) was transferred from previous NMR studies of Grb2 by Yuzawa et al.<sup>[60]</sup> (BMRB-ID: 5693) and Sanches et al.<sup>[61]</sup> (BMRB-ID: 27781) and confirmed with the help of a  $^1\text{H}-^{15}\text{N}$  HSQC-TOCSY experiment. The resonance assignment of the  $^1\text{H}-^{15}\text{N}$  HSQC spectrum of peptide-bound Grb2 SH2 was taken from Ogura et al.<sup>[62]</sup> (BMRB-ID: 11055). We assured binding of pYXN peptides to Grb2 SH2 by performing titrations of Grb2 SH2 with the individual pYXN peptides and measuring CSPs. Figure S7 shows the series of HSQC spectra recorded during titration with pYVN (Fig S7A), pYKN (Fig S7B), and pYEN (Fig S7C). We observed CSPs ( $>0.2$  ppm) for several residues, a disappearing of peaks at concentrations of 40–60 mol% peptide, and a reappearing of peaks at concentrations of  $\geq 100$  mol% peptide. This indicates that ligand binding happens in slow exchange on the NMR time scale and that pYXN peptides have a high binding affinity. Figure S8 shows the CSPs induced by pYVN (Fig S8A), pYKN (Fig S8B), and pYEN (Fig S8C) plotted along the Grb2 SH2 residue number. Mapping of the most significant CSPs on the molecular surface of Grb2 SH2 allowed unambiguous identification of the peptide binding region (right side in Fig S8). The CSP-derived binding regions are in perfect agreement with our docking and MD simulation derived models of the individual Grb2 SH2/peptide complexes (Figure 4). The largest CSPs were measured for residues that line the peptide binding pocket and are located in the  $\beta$ 1– $\beta$ 2 loop,  $\beta$ 2 strand,  $\beta$ 3 strand, and the  $\beta$ 3– $\alpha$ 2 loop.

For measuring  $^1\text{H}_N$  PRE rates, we used 5-fold molar excess of peptide, at which the binding site on Grb2 SH2 is fully saturated, and either cationic aminomethyl-PROXYL ( $\Gamma_{2,+}$ ) or neutral carbamoyl-PROXYL ( $\Gamma_{2,n}$ ) at a concentration of 9.8 mM. We also tested anionic carboxy-PROXYL, but the quality of the Grb2 SH2 NMR spectrum deteriorated significantly at concentrations of carboxy-PROXYL above 3.5 mM. This prevented us from measuring significantly high PREs in the presence of carboxy-PROXYL. However, we observed pronounced signal intensity changes of several NMR signals of Grb2 SH2 in the

presence of 9.8 mM aminomethyl-PROXYL and carbamoyl-PROXYL, respectively. A comparison of the intensity of selected HSQC signals of Grb2 SH2 in the absence (apo) and presence of pYXN peptides is shown in Figure 5A and Fig S9. In the apo state, we observed strong PREs for residues that are part of or near the pYXN binding site, e.g., E89, S90 (both  $\beta$ 1– $\beta$ 2 loop), Q106, K109 (both  $\beta$ 3 strand), and W121 ( $\beta$ 3– $\alpha$ 2 loop). For S90 the HSQC signal is broadened beyond detection by the paramagnetic aminomethyl-PROXYL indicating a very high PRE rate. The small remaining signals of E89 and Q106 challenged the detection limit but allowed to determine a PRE rate (see also Fig S9). Furthermore, the HSQC signals of K109 and W121 are significantly reduced in their intensity by both aminomethyl-PROXYL and carbamoyl-PROXYL. The  $\Gamma_{2,+}$  and  $\Gamma_{2,n}$  rates calculated from the signal intensity changes are plotted along the Grb2 SH2 amino acid sequence in Figure 5B. The named HSQC signals reappeared upon addition of each pYXN peptide (Fig S9) and a reduction of the PREs of those residues was observed with both tested PROXYLs. This effect was the same for all three peptides – pYVN, pYKN, and pYEN (Figure 5B and S10) – and could indicate that the accessibility of the Grb2 SH2 surface for the PROXYL probes was blocked by the peptide ligands, thus increasing the protein-PROXYL distance and decreasing the PRE for residues within the peptide binding site. In contrast, residues that are outside of the peptide binding site showed no signal intensity modulating effect in the presence of pYXN peptides. This is exemplified shown for G93 in Figure 5A. The PRE rates of residues outside of the peptide binding site were almost the same in the free and peptide-bound state, indicating that the peptide ligand does not affect the accessibility of those residues to the PROXYL probes.

To aid the structural interpretation of the PRE data, we plotted them on the molecular surface of Grb2 SH2 shown in Fig 6 and Fig S11. We compared the strength and distribution pattern of  $\Gamma_{2,+}$  and  $\Gamma_{2,n}$  rates of the apo state (Figure 6A) with those of the pYVN-bound state (Figure 6B) as well as the other peptide-bound states (Fig S11). In addition, we calculated the PRE differences ( $\Delta\Gamma_{2,+}$ ,  $\Delta\Gamma_{2,n}$ ) between peptide-bound and apo states and analyzed their distribution patterns. Figure 6C displays the PRE differences versus the Grb2 SH2 residue number for the pYVN-bound state and Figure 6D shows protein surface mappings of the  $\Delta\Gamma_{2,+}$  and  $\Delta\Gamma_{2,n}$  rates. The PRE differences for all peptide-bound states and their protein surface mappings are shown in Fig S12 in the supplement. As can be seen in Fig 6 and Fig S12, PREs change most significantly within a narrow surface region of Grb2 SH2. This area (encircled by a red line in Figure 6) corresponds to the binding site of pYVN. Also for the pYKN- and pYEN-bound states, PREs are most strongly reduced in this surface region of the Grb2 SH2 structure (Fig S11+S12). Intriguingly, the pattern of PRE changes resembles very closely the pattern of CSPs (Fig S8). These findings support our previous interpretation that the peptide ligand sterically blocks access of the PROXYL probes to the protein surface within a defined region, which corresponds to the ligand binding site. Thus, the PRE data provide precise information about the location of the pYXN peptide binding site. We suppose that this approach may be applicable also to

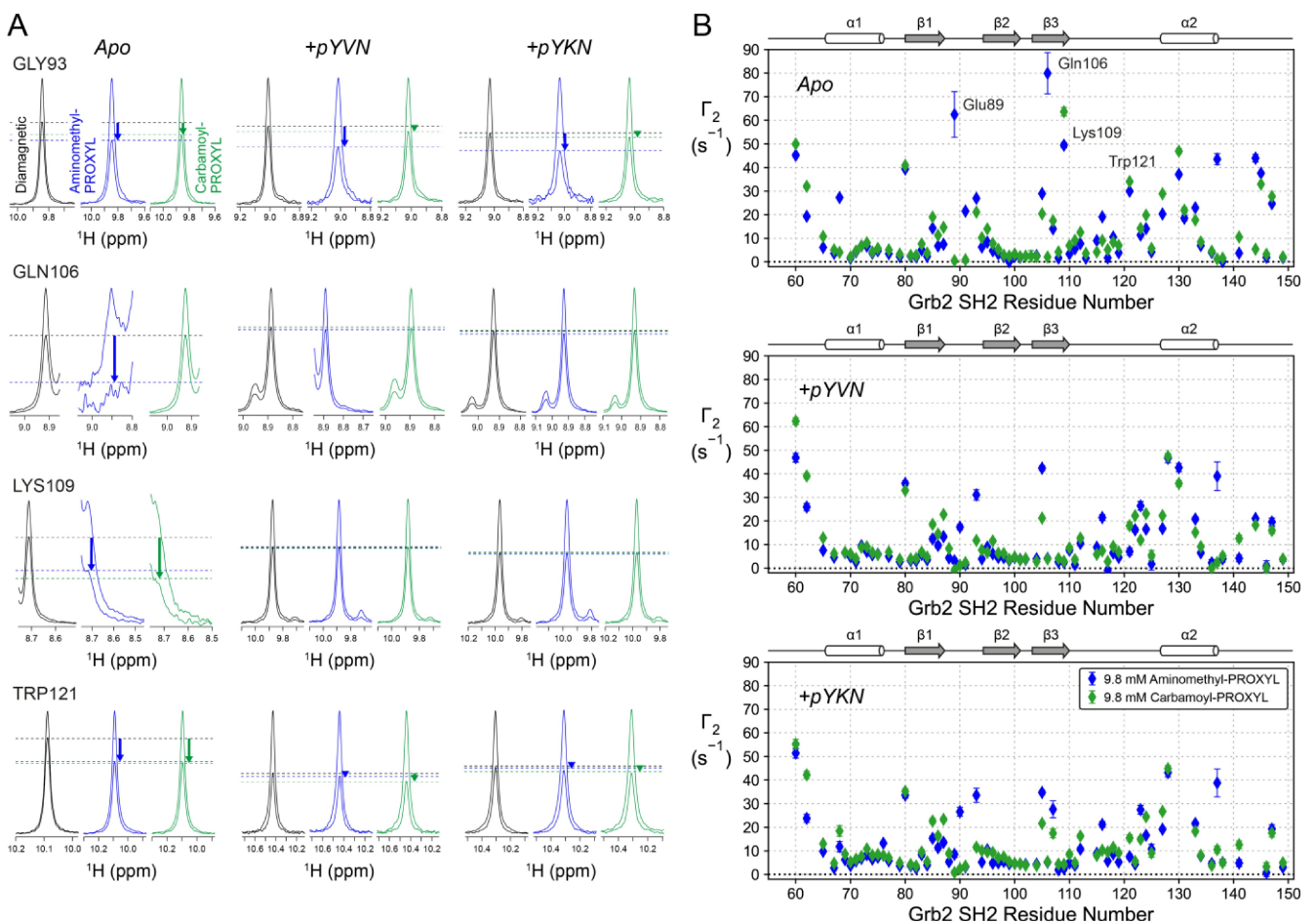


**Figure 5.** Paramagnetic NMR data used to analyze the electrostatic potentials around Grb2 SH2 and Grb2 SH2/peptide complexes. (A) Examples of signal intensity changes used to measure <sup>1</sup>H<sub>N</sub> PRE rates of Grb2 SH2 apo protein and Grb2 SH2 in the presence of pYVN or pYKN peptide, respectively. The <sup>1</sup>H slices of the <sup>1</sup>H-<sup>15</sup>N HSQC signals of G93, Q106, K109, and W121 of Grb2 SH2 at 0 ms and 10 ms relaxation measurement delays are plotted. The <sup>1</sup>H signal slices in the absence (diamagnetic, black) or presence of 9.8 mM aminomethyl-PROXYL (paramagnetic, blue) or carbamoyl-PROXYL (paramagnetic, green) normalized to the intensity at 0 ms are displayed. Signal change differences observed in the presence of PROXYL derivatives relative to the diamagnetic case are indicated with arrows. (B) <sup>1</sup>H<sub>N</sub> PRE rates  $\Gamma_{2,+}$  (blue) and  $\Gamma_{2,n}$  (green) of Grb2 SH2 in the absence and presence of pYVN or pYKN peptide, respectively, versus the Grb2 SH2 residue number. The signal intensity changes and <sup>1</sup>H<sub>N</sub> PRE rates measured in the presence of pYEN peptide were very similar to those in the presence of pYVN or pYKN, and are shown in Fig S10. Error bars represent the  $\Gamma_2$  rate uncertainties (see Experimental Section). All <sup>1</sup>H<sub>N</sub> PRE rates of Grb2 SH2 are summarized in Table S2 in the supporting material.

other protein-ligand systems and that PRE data derived from soluble PROXYL probes can be in general helpful for the spatial mapping of ligand binding sites.

#### NMR-determined electrostatic potentials for Grb2 SH2 and Grb2 SH2/peptide complexes

To analyze how pYXN peptides affect the electrostatic potential of Grb2 SH2, we determined  $\phi_{ENS}$  from the measured  $\Gamma_{2,+}$  and  $\Gamma_{2,n}$  rates (Figure 5B, Table S2) by applying equation 1. We obtained  $\phi_{ENS}$  values for 57 residues of Grb2 SH2 in the apo state, and for 53, 56, and 51 residues of Grb2 SH2 in the pYVN-, pYKN-, and pYEN-bound state, respectively. Figure 7 shows the NMR derived  $\phi_{ENS}$  data (black) for Grb2 SH2 and Grb2 SH2/peptide complexes. For comparison with the experimental  $\phi_{ENS}$  values, we also calculated the theoretical  $\phi_{ENS}$  values using the APBS computed potential grids and the MD-derived models of

Grb2 SH2 or Grb2 SH2/peptide complexes (Figure 4). The theoretical  $\phi_{ENS}$  data (red) are plotted as average  $\pm$  S.D. along the residue number and correlated with the experimental  $\phi_{ENS}$  values in Figure 7. The agreement between experimental and theoretical data was fairly good, with RMSD values in secondary structure regions of 4.8 mV (Grb2 SH2), 6.2 mV (Grb2 SH2/pYVN), 6.5 mV (Grb2 SH2/pYKN), and 7.2 mV (Grb2 SH2/pYEN). The correlation coefficients were 0.70 (Grb2 SH2), 0.59 (Grb2 SH2/pYVN), 0.58 (Grb2 SH2/pYKN), and 0.66 (Grb2 SH2/pYEN). However, several outliers were observed for residues in loop regions, e.g., G93 ( $\beta_1$ - $\beta_2$  loop), V105 ( $\beta_2$ - $\beta_3$  loop), A115, G116, Y118, W121, V123 (all  $\beta_3$ - $\alpha_2$  loop), and S141 (tail after  $\alpha_2$ ). The discrepancy between experimental and predicted  $\phi_{ENS}$  data could be explained by increased conformational flexibility for these parts of the Grb2 SH2 structure. In particular, the  $\beta_3$ - $\alpha_2$  loop showed increased flexibility in the MD simulation, resulting in standard deviations of  $\phi_{ENS}$  of up to 10 mV for this loop. The lack of agreement would make it difficult to use  $\phi_{ENS}$  values

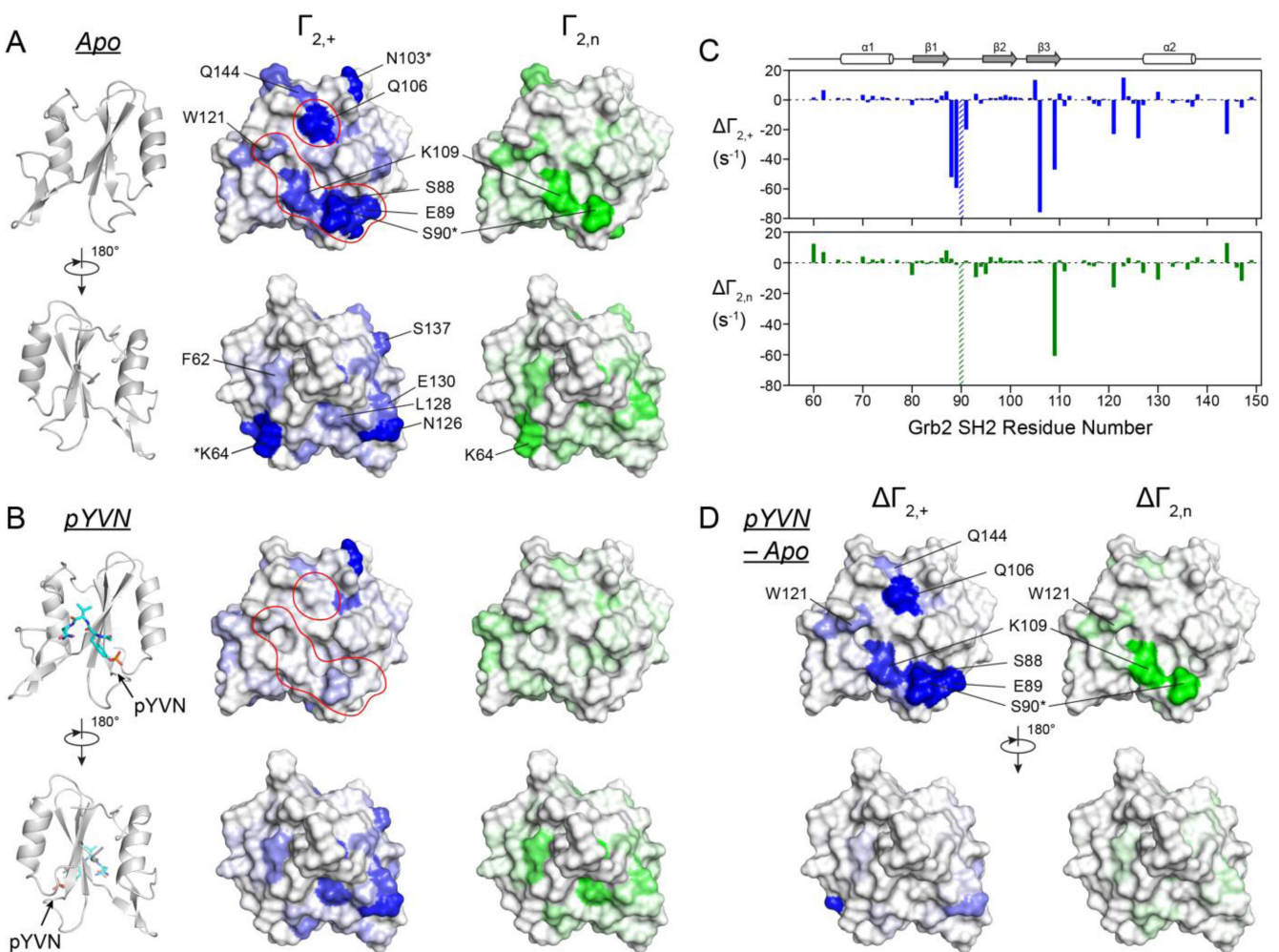


**Figure 6.**  $^1\text{H}_\text{N}$  PRE rates measured for Grb2 SH2 in the presence of either aminomethyl-PROXYL ( $\Gamma_{2,+}$ ) or carbamoyl-PROXYL ( $\Gamma_{2,n}$ ) are plotted on the molecular surface of Grb2 SH2. (A)  $\Gamma_{2,+}$  and  $\Gamma_{2,n}$  rates for Grb2 SH2 apo protein. Residues with high PRE rates in the apo dataset are labeled. Residues whose signal was wiped out in the presence of PROXYLs are labeled with an asterisk (\*). (B)  $\Gamma_{2,+}$  and  $\Gamma_{2,n}$  rates for Grb2 SH2 bound to pYVN. The region in which strong PRE rates disappear is framed with a red line. (C) Difference of PRE rates between apo and pYVN-bound state ( $\Delta\Gamma_{2,+}$ ,  $\Delta\Gamma_{2,n}$ ) are plotted versus the Grb2 SH2 residue number. The difference PRE rates are defined as:  $\Delta\Gamma_{2,+} = \Gamma_{2,+}(\text{pYVN}) - \Gamma_{2,+}(\text{apo})$  and  $\Delta\Gamma_{2,n} = \Gamma_{2,n}(\text{pYVN}) - \Gamma_{2,n}(\text{apo})$ . The dashed bars at residue S90 indicate that this signal was wiped out by the PROXYL compounds in the apo state but not in the pYVN-bound state, indicating a significant decrease of the  $\Gamma_{2,+}$  and  $\Gamma_{2,n}$  rates. (D) The absolute values of  $\Delta\Gamma_{2,+}$  and  $\Delta\Gamma_{2,n}$  are plotted on the surface of Grb2 SH2. Residues with high difference PRE rates are labeled. The strength of PRE rates is indicated with a color gradient.  $\Gamma_{2,+}$  or  $\Delta\Gamma_{2,+}$ : 0 Hz (white) – 60 Hz (blue),  $\Gamma_{2,n}$  or  $\Delta\Gamma_{2,n}$ : 0 Hz (white) – 60 Hz (green). Grb2 SH2 is shown from two different perspectives. Additional surface mappings of  $\Gamma_2$  and  $\Delta\Gamma_2$  rates measured for Grb2 SH2 in the presence of pYKN or pYEN are shown in supporting Figures S11 and S12.

quantitatively as restraints for structure prediction tasks, by evaluating the match between experimental and back-calculated  $\phi_{\text{ENS}}$  data. However, further studies are still needed to assess the predictive power of  $\phi_{\text{ENS}}$  data for modeling protein-ligand interactions and establish best practices how to translate  $\phi_{\text{ENS}}$  data into structural information. One possibility could be to obtain information on the location of the ligand binding site by comparing the  $\phi_{\text{ENS}}$  data collected for the ligand-bound and ligand-free states, similarly to our analysis of the PRE differences. As demonstrated in the previous section, the location of the largest  $\Delta\Gamma_2$  rates could be used to precisely narrow down the location of the pYXN binding site in Grb2 SH2 (Figure 6). This kind of information can be very useful as a starting point for modeling of a protein-ligand complex. Looking at the  $\phi_{\text{ENS}}$  curve of Grb2 SH2 and comparing it with those of the Grb2

SH2/peptide complexes (Figure 7), some small but clear differences can be observed. In Figure 8 only the section of the  $\phi_{\text{ENS}}$  curve from K100 to L120 is plotted. It can be seen that the  $\phi_{\text{ENS}}$  curve is shifted to smaller  $\phi_{\text{ENS}}$  values for each pYXN peptide compared to the case without peptide. The downshift of the  $\phi_{\text{ENS}}$  curve is most pronounced for pYVN and pYEN peptides, which carry net charges of  $-2e$  and  $-3e$ , respectively, and less pronounced for pYKN, which has a more positive charge of  $-1e$ . This finding suggests that the pYXN peptides change the  $\phi_{\text{ENS}}$  potential locally in a narrow region of Grb2 SH2. This region corresponds to the  $\beta_3$  strand and the first loop after  $\beta_3$ . Both parts of the Grb2 SH2 structure establish direct contacts with the peptide ligand, which could explain why  $\phi_{\text{ENS}}$  is changed in this region.

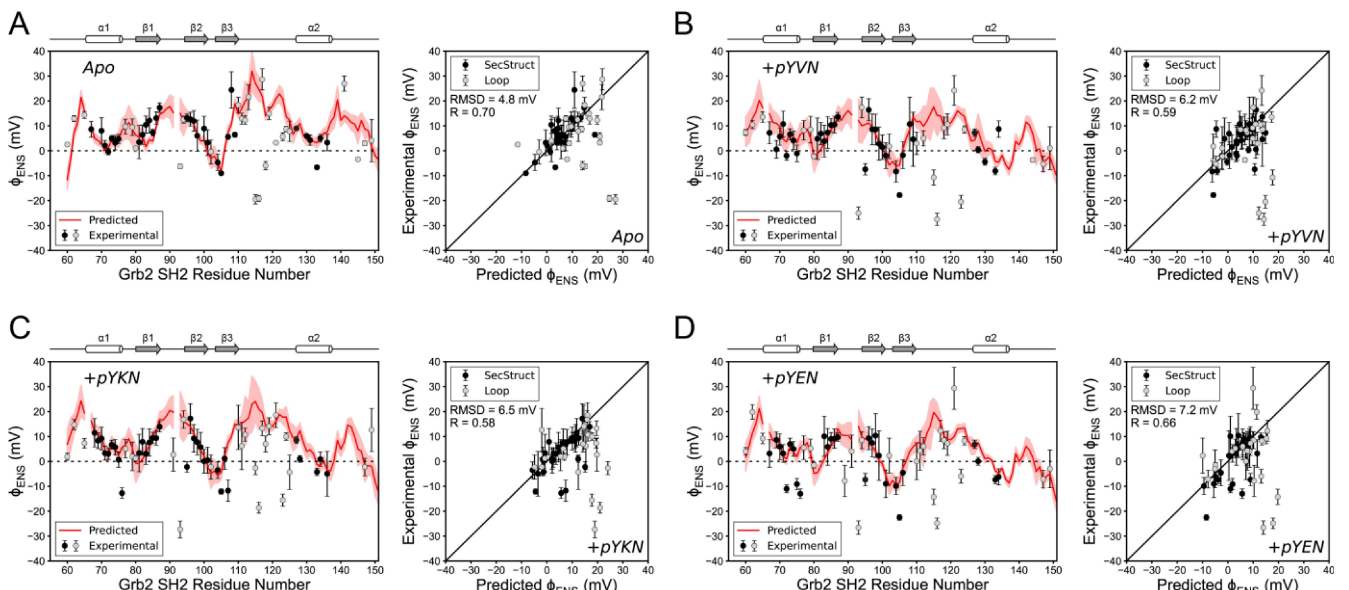


**Figure 7.** ENS electrostatic potentials determined from the  $^1\text{H}$  PRE NMR data of Grb2 SH2 and Grb2 SH2/peptide complexes. Experimentally determined (black and gray points) and predicted ENS potentials (red line) versus residue number plots and experimental versus predicted  $\phi_{\text{ENS}}$  data plots for (A) Grb2 SH2 apo, (B) Grb2 SH2 with pYVN, (C) Grb2 SH2 with pYKN, and (D) Grb2 SH2 with pYEN. The predicted  $\phi_{\text{ENS}}$  values represent the mean of the ENS potentials calculated from a 100 ns MD simulation of Grb2 SH2 or Grb2 SH2/peptide complexes. The red shaded area indicates the standard deviation of the  $\phi_{\text{ENS}}$  predictions. Data points for residues located in secondary structure regions are shown in black and those for residues in loop regions are shown in gray. Error bars represent the experimental  $\phi_{\text{ENS}}$  value uncertainties (see Experimental Section).

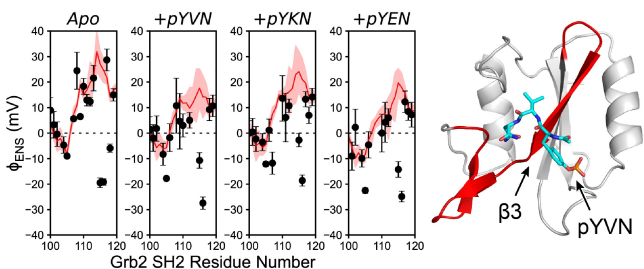


**Figure 8.** ENS electrostatic potential for residues 100 to 120 in Grb2 SH2 is reduced by the presence of pYXN peptides – pYVN ( $q = -2e$ ), pYKN ( $q = -e$ ), pYEN ( $q = -3e$ ). Left: Experimentally determined (black points) and predicted ENS potentials (red line) versus residue number. Right: Molecular model of Grb2 SH2 with pYVN. The ribbon segment corresponding to residues 100–120 is colored red.

Together, our data show that the  $\phi_{\text{ENS}}$  potential of Grb2 SH2 can be measured using paramagnetic NMR in good agreement with theoretical predictions. The effect of pYXN peptides on  $\phi_{\text{ENS}}$  is localized to a narrow region on the protein. This kind of information could be useful for ligand binding mode discovery.

## Conclusions

Paramagnetic NMR methods represent an important NMR tool employed in drug discovery and drug development. They can provide structural restraints for modeling the structure of protein-ligand complexes, even for weakly interacting ligands. However, the covalent labeling of proteins with paramagnetic tags or the generation of metal ion-tagged ligands is complicated and bears the risk of perturbing the protein

structure and/or ligand binding mode. Experiments with paramagnetic cosolutes offer a promising alternative because they require no chemical modification of protein or ligand. Instead, the paramagnetic probes can be directly added to the protein solution. The PROXYL probes used in the present study have small size, which lowers the risk of unspecific binding to the protein. Moreover, the differently charged sidechains of the PROXYL probes influence their distribution around the protein, which offers flexibility in tuning the size of the solvent PRE effect.

Using two test systems, the proteins IL-8 and Grb2 SH2, we have evaluated the utility of the PROXYL method for mapping ligand binding sites in proteins and for measuring the effect of ligand binding on the electrostatic potential of proteins. Our study extends and completes previous investigations, which reported the *de novo* determination of  $\phi_{\text{ENS}}$  for proteins<sup>[31,63]</sup> and DNA<sup>[33]</sup> as well as studies, which mapped interfaces in protein-protein complexes using soluble, Gd<sup>3+</sup>-chelating paramagnetic agents.<sup>[29,30]</sup>

Our NMR-determined  $\phi_{\text{ENS}}$  data for IL-8 and two IL-8/GAG complexes show that a highly negatively charged HP ligand reduced the  $\phi_{\text{ENS}}$  of IL-8, in agreement with theoretical predictions from APBS calculations, while a less charged HA ligand had only a negligible effect on  $\phi_{\text{ENS}}$ .

The results for Grb2 SH2 and three Grb2 SH2/peptide complexes show that the PROXYL-induced PRE data allow a precise localization of the peptide binding region. The location of the peptide binding region obtained by the PROXYL method matches the region inferred from CSP data and agrees well with the crystallographic binding pose of phosphotyrosine peptides on Grb2 SH2.<sup>[59]</sup> Furthermore, the effect on  $\phi_{\text{ENS}}$  was localized to

a narrow region in Grb2 SH2, as expected from the small size of the pYXN tripeptide ligands.

Information on how interacting ligand and drug molecules shape  $\phi_{ENS}$  is important for understanding the protein-ligand interaction mechanism and could give insights into the biological responses that are triggered by the ligand recognition process. Our results show that experiments with soluble, paramagnetic PROXYL probes can be a useful addition to the toolbox of NMR methods for studying protein-ligand interactions. NMR-determined  $\phi_{ENS}$  data could be useful for comparison with computational predictions of protein-ligand electrostatics-driven interactions. In addition, PRE data-derived ligand binding sites can serve as general constraints to guide protein-ligand structure calculations or can be used as filters to validate generated protein-ligand models.

## Experimental Section

**Proteins and other materials:**  $^{15}\text{N}$ -labeled IL-8(1-77) (excluding the first 22-amino acid signal peptide from the Uniprot sequence P10145) was expressed in *E. coli* strain ER2566 and purified as described by Pichert et al.<sup>[44]</sup> Please note the difference of –5 residues in the nomenclature when comparing to IL-8(1-72).  $^{15}\text{N}$ -labeled Grb2 SH2 domain (comprising residues M55-D150 of Grb2 from Uniprot sequence P62993; cloned in pET21b(+) plasmid) was expressed in *E. coli* strain Rosetta (DE3) at 20 °C for 16 hours after induction with 0.4 mM IPTG and was purified by Ni-NTA affinity chromatography and size exclusion chromatography as described in the Supporting Information. The PROXYL derivatives 3-amino-methyl-PROXYL, 3-carboxy-PROXYL, and 3-carbamoyl-PROXYL were purchased from Sigma-Aldrich. The phospho-peptides Ac-pTyr-Val-Asn-NH<sub>2</sub>, Ac-pTyr-Glu-Asn-NH<sub>2</sub>, and Ac-pTyr-Lys-Asn-NH<sub>2</sub> were synthesized by the Leipzig University peptide synthesis core unit using standard F-moc solid phase synthesis strategy. Peptide identity was confirmed by MALDI-TOF mass spectrometry. Heparin (HP) and hyaluronan (HA) hexasaccharides (dp6, where dp stands for the degree of polymerization) were purchased from Iduron (Manchester, UK).

**NMR sample preparation:** NMR samples of  $^{15}\text{N}$ -labeled IL-8 contained 0.33 mM protein in IL-8 sample buffer (20 mM Na-phosphate (pH 7.0), 40 mM NaCl, 10 mM DMSO, and 5% D<sub>2</sub>O). NMR samples of IL-8 with HP contained 0.40 mM protein and 0.40 mM HP dp6 in IL-8 sample buffer, and NMR samples of IL-8 with HA contained 0.29 mM protein and 1.0 mM HA dp6. Samples were prepared by stepwise titration of IL-8 with GAGs and the titration was followed by recording a  $^1\text{H}$ - $^{15}\text{N}$  HSQC spectrum for each step. The paramagnetic NMR samples of IL-8 with PROXYLs contained 9.5 mM of either 3-aminomethyl-PROXYL or 3-carboxy-PROXYL. The diamagnetic IL-8 sample was prepared by adding sample buffer containing no PROXYLs to achieve the same concentration of IL-8 or IL-8+GAGs as in the case of the paramagnetic sample. NMR samples of Grb2 SH2 domain contained 0.24 mM protein in Grb2 SH2 sample buffer (20 mM Tris-HCl (pH 7.2), 100 mM NaCl, 10 mM DMSO, and 5% D<sub>2</sub>O). NMR samples of Grb2 SH2 domain with phospho-peptides contained 0.24 mM protein and 1.2 mM of either Ac-pYVN-NH<sub>2</sub>, Ac-pYEN-NH<sub>2</sub>, or Ac-pYKN-NH<sub>2</sub> peptide, respectively. The paramagnetic NMR samples of Grb2 SH2 with or without phospho-peptides contained 9.8 mM 3-aminomethyl-PROXYL or 3-carbamoyl-PROXYL, respectively. The diamagnetic control sample was prepared by adding sample buffer containing no PROXYLs until the same concentration of Grb2 SH2 or Grb2 SH2+peptide as in the case of the paramagnetic sample was reached. The preparation

and quantification of the PROXYL stock solutions is described in the Supporting Information.

**NMR experiments:** The binding of GAGs to IL-8 and of phosphopeptides to Grb2 SH2 during titrations with ligands were followed by recording  $^1\text{H}$ - $^{15}\text{N}$  HSQC spectra.<sup>[64]</sup> Spectra were acquired typically with spectral widths of 16 ppm for  $^1\text{H}$  and 38 ppm for  $^{15}\text{N}$  as well as 128–256 data points in the indirect dimension. The NMR resonance assignment of the  $^1\text{H}$ - $^{15}\text{N}$  HSQC spectrum of IL-8 was taken from Pichert et al.<sup>[44]</sup> The resonance assignment of the  $^1\text{H}$ - $^{15}\text{N}$  HSQC spectrum of the apo form of Grb2 SH2 was transferred from Yuzawa et al.<sup>[60]</sup> (BMRB-ID: 5693) and Sanches et al.<sup>[61]</sup> (BMRB-ID: 27781). NMR signal assignments were confirmed with the help of a 3D  $^1\text{H}$ - $^{15}\text{N}$  HSQC-TOCSY spectrum of apo Grb2 SH2 acquired at a  $^1\text{H}$  field strength of 700 MHz and a TOCSY mixing time of 60 ms. The resonance assignment of the  $^1\text{H}$ - $^{15}\text{N}$  HSQC spectrum of peptide-bound Grb2 SH2 was transferred from Ogura et al.<sup>[62]</sup> (BMRB-ID: 11055). The PRE rates of the  $^1\text{H}$  transverse magnetizations ( $\Gamma_2$ ) of the protein  $^1\text{H}_N$  nuclei were measured using a  $^1\text{H}$ - $^{15}\text{N}$  HSQC experiment with a spin echo sequence implemented during the first INEPT period.<sup>[65]</sup> The two time-point approach<sup>[65]</sup> with a 10-ms difference was chosen and the two spectra were recorded in an interleaved manner. For each protein and ligand, the PRE experiments were conducted with three samples: one diamagnetic reference sample, containing no PROXYL derivative, and two paramagnetic samples, one containing 3-amino-methyl-PROXYL, and the other one containing either 3-carboxy-PROXYL or 3-carbamoyl-PROXYL. Uncertainties in  $\Gamma_2$  rates were estimated using an error propagation procedure.<sup>[65]</sup> All NMR experiments on IL-8 were performed at 30 °C using a Bruker NEO 700 MHz spectrometer equipped with a 5 mm E-free HCN triple resonance probe. All NMR experiments on Grb2 SH2 were performed at 25 °C using a Bruker Avance III 600 MHz spectrometer quipped with a 5 mm inverse triple resonance probe with z-gradient. The Bruker software Topspin™ was used for data acquisition and spectrum processing. Analysis of the NMR spectra and quantification of the NMR signal intensities for PRE measurements was carried out using the NMRFAM-SPARKY software.<sup>[66]</sup>

**Determination of NMR-based near-surface electrostatic potentials:** The ENS electrostatic potentials  $\varphi_{ENS}$  of individual  $^1\text{H}_N$  nuclei were determined from the  $\Gamma_2$  rates using equation (1), which was derived by Yu et al.<sup>[31]</sup>

$$\phi_{ENS} = \frac{k_B T}{(z_b - z_a)e} \ln \left( \frac{\Gamma_{2,a}}{\Gamma_{2,b}} \right) \quad (1)$$

where  $k_B$  is the Boltzmann constant;  $T$  is temperature;  $e$  is the elementary charge;  $z$  is a charge valence of a PROXYL derivative; and suffixes  $a$  and  $b$  refer to the two PROXYL derivatives. Since a neutral pH was used for the PRE measurements,  $z=+1$  for 3-aminomethyl-PROXYL,  $z=0$  for 3-carbamoyl-PROXYL, and  $z=-1$  for 3-carboxy-PROXYL. The uncertainties in  $\varphi_{ENS}$  were estimated using an error propagation protocol as described in Yu et al.<sup>[31]</sup> We used the selection criteria described in Yu et al.<sup>[31]</sup> to use only statistically significant  $\Gamma_2$  rates and  $\Gamma_{2,a}/\Gamma_{2,b}$  rates for calculation of  $\varphi_{ENS}$ .

**Molecular structures:** The structure of dimeric IL-8 was obtained from the Protein Data Bank (PDB ID: 1IL8, NMR structure).<sup>[54]</sup> Missing N-terminal residues were added in the xLeap module of AMBER20.<sup>[67]</sup> The structure of Grb2 SH2 was obtained from the PDB (PDB ID: 1JYR, 1.55 Å).<sup>[59]</sup> An eight-residue long histidine tag (LEH<sub>8</sub>) was added in xLeap to the protein sequence to match the exact sequence of the protein used in the presented NMR experiments. The GAG ligand structures were extracted from the PDB (PDB ID: 1HPN<sup>[68]</sup> and 2BVK,<sup>[69]</sup> NMR structures), for HP dp6 and HA dp6,

respectively. Three tripeptide ligands Ac-pYXN-NH<sub>2</sub> (X=V, E, or K) containing a phosphotyrosine residue (pY), were constructed based on the peptide ligand from (PDB ID: 1JYR, 1.55 Å).<sup>[59]</sup>

**Molecular docking:** Molecular docking was performed using Autodock3.<sup>[70]</sup> The docking simulation of IL-8/HP and IL-8/HA complexes used a grid box of size 60 Å×60 Å×60 Å with a grid step of 0.375 Å, centered on the two α-helices of dimeric IL-8. The docking of each complex was carried out in 100 independent runs using the Lamarckian Genetic Algorithm for 10<sup>5</sup> generations, an initial population size of 300, and 9995 × 10<sup>5</sup> energy evaluations. The 50 docking poses with the best Autodock3-score were clustered using the DBSCAN algorithm.<sup>[71]</sup> Ten cluster representatives per IL-8/GAG complex with the best Autodock3-score were used for subsequent analyses.

**Molecular dynamics simulations:** All MD simulations were carried out in AMBER<sup>[67]</sup> using the ff14SBonlySC<sup>[72]</sup> force field parameters for proteins, and GLYCAM06<sup>[73]</sup> force field parameters for GAG ligands. The starting structures of IL-8 and Grb2 SH2 were obtained from the aforementioned PDB files. The cluster representatives previously identified for the IL-8/GAG docking models were used as starting structures of the MD simulations of the IL-8/GAG complexes, resulting in 10 MD systems per complex. The IL-8/HP and IL-8/HA systems were solvated using a truncated octahedron TIP3P periodic box with 15.0 Å distance between the complex and the box boundaries. The starting structures of the Grb2 SH2/peptide complexes were obtained by substituting the ligand in the PDB 1JYR with the phosphotyrosine-containing Ac-pYXN-NH<sub>2</sub> (X=V, E, K) ligands. The ff14SBonlySC<sup>[72]</sup> force field parameters in AMBER were used, together with appropriate parameters for the phosphorylated tyrosine residues.<sup>[74]</sup> Each structure was placed in a TIP3P water box whose boundaries were at a 15.0 Å distance from the complex atoms.

All analyzed systems were neutralized by adding Na<sup>+</sup>/Cl<sup>-</sup> counterions prior to the MD simulations. A two-step energy minimization protocol was used, where the first step contained 0.5×10<sup>3</sup> steepest descent cycles and 10<sup>3</sup> conjugate cycles with harmonic force restraints on solute atoms (100 kcal/mol/Å<sup>2</sup>), and the second step contained 3×10<sup>3</sup> steepest descent cycles and 3×10<sup>3</sup> conjugate gradient cycles without restraints. The system was then heated up to 300 K for 10 ps using a Langevin thermostat (collision frequency 1 ps<sup>-1</sup>), followed by an equilibration step at 300 K in an isothermal isobaric ensemble for 100 ns. The subsequent MD production run was carried out for 100 ns, employing the Particle Mesh Ewald method for the computation of long-range electrostatic interactions and the SHAKE algorithm for constraining all covalent bonds involving hydrogen atoms. The resulting trajectories were visualized in VMD.<sup>[75]</sup> The cpptraj module from AMBER was used for the analysis of the obtained trajectories.<sup>[76]</sup>

All frames of the MD trajectories were analyzed using Molecular Mechanics-Generalized Born Surface Area (MM-GBSA) in AMBER20 with igb=2.<sup>[77]</sup> Out of the ten trajectories obtained per IL-8/GAG complex, a representative MD simulation was chosen based on the lowest binding free energy value, followed by visual inspection and analysis of the obtained trajectories in the context of known binding poses of HP in complex with IL-8.

**Poisson-Boltzmann equation-based calculation of electrostatic potentials:** For each MD trajectory of the IL-8/GAG and Grb2 SH2/peptide complexes, 100 configurations equally spaced throughout the 100 ns trajectory were extracted and converted to individual PQR files using the xLeap module of AMBER<sup>[67]</sup> and the Open Babel chemical toolbox.<sup>[78]</sup> The Adaptive Poisson-Boltzmann Solver (APBS) software<sup>[55,56]</sup> was used to create the electrostatic potential surface maps. Additional electrostatic potential maps were obtained for the

apo structures of IL-8 and Grb2 SH2. Atomic radii and charges were assigned using the AMBER ff14SBonlySC<sup>[72]</sup> force field parameters. Each system was placed in a 144 Å×144 Å×144 Å box with a spacing of 0.5 Å, resulting in 289×289×289 grid points. The monovalent ion concentration was set to 70 mM or 100 mM, respectively, to reflect the actual ionic strength in the IL-8 or Grb2 SH2 sample buffers. The solvent van der Waals radius was set to 1.4 Å and the ionic radius was fixed at 2.0 Å. The dielectric constant of solvent and protein interior was set to 78 and 2, respectively. The theoretical ENS electrostatic potentials  $\varphi_{ENS}$  of individual <sup>1</sup>H<sub>N</sub> nuclei were calculated from the electrostatic potential values at all grid points which were outside of the space occupied by protein and ligand using equations (1) and (2):

$$\frac{\Gamma_{2,a}}{\Gamma_{2,b}} = \sum_i a_i r_i^{-6} \exp\left(\frac{U_{a,i}}{k_B T}\right) / \sum_i a_i r_i^{-6} \exp\left(\frac{U_{b,i}}{k_B T}\right) \quad (2)$$

where  $i$  is the index of a grid point,  $U$  is the electrostatic potential at the grid point  $i$ ,  $r_i$  is the distance between that grid point and a <sup>1</sup>H<sub>N</sub> nucleus, and  $a_i$  is the accessibility of that grid point (0 for inaccessible grid points, 1 for accessible grid points). The accessibility of a grid point for the paramagnetic PROXYL probe was assessed by comparing the van der Waals radii of protein and ligand atoms to an empirically determined accessibility radius of 3.5 Å for the PROXYL probe. This value was found optimal by Yu et al.<sup>[31]</sup> in yielding the best agreement between experimental and predicted  $\varphi_{ENS}$  data. Thus, grid points that were closer to a protein or ligand atom than the sum of the atom van der Waals radius and PROXYL probe accessibility radius were considered to lie in the inaccessible interior of the macromolecule, and otherwise in the accessible exterior. The computation of the  $\varphi_{ENS}$  data from the APBS output grids was conducted using a Python script.

## Acknowledgements

This work was supported by the Deutsche Forschungsgemeinschaft (Project numbers TRR-386/A2 and TRR-386/B2 to GK) and the National Science Centre of Poland (Narodowe Centrum Nauki, grant number UMO-2018/31/G/ST4/00246 to SS, AD and MG). AP and DH acknowledge DFG funding through project 426256511. We acknowledge further funding from the Open Access Publishing Funds of Leipzig University supported by the German Research Foundation within the program Open Access Publication Funding. We thank the Polish high-performance computing infrastructure PLGrid (HPC Centers: ACK Cyfronet AGH) for providing computer facilities and support within computational grant no. PLG/2020/014275. Open Access funding enabled and organized by Projekt DEAL.

## Conflict of Interests

The authors declare no conflict of interest.

## Data Availability Statement

The data that support the findings of this study are available in the supplementary material of this article.

**Keywords:** NMR spectroscopy · protein-ligand interactions · nitroxides · solvent paramagnetic relaxation enhancements · molecular dynamics

- [1] A. Furukawa, T. Konuma, S. Yanaka, K. Sugase, *Prog. Nucl. Magn. Reson. Spectrosc.* **2016**, *96*, 47–57.
- [2] W. Becker, K. C. Bhattacharlu, N. Gubensák, K. Zanger, *ChemPhysChem* **2018**, *19*, 895–906.
- [3] Y. Mizukoshi, K. Takeuchi, Y. Tokunaga, H. Matsuo, M. Imai, M. Fujisaki, H. Kamoshida, T. Takizawa, H. Hanzawa, I. Shimada, *Sci. Adv.* **2020**, *6*, eabd0480.
- [4] E. Skeens, G. P. Lisi, *Methods* **2023**, *209*, 40–47.
- [5] M. Mayer, B. Meyer, *J. Am. Chem. Soc.* **2001**, *123*, 6108–6117.
- [6] C. B. Post, *Curr. Opin. Struct. Biol.* **2003**, *13*, 581–588.
- [7] C. Dalvit, G. Fogliatto, A. Stewart, M. Veronesi, B. Stockman, *J. Biomol. NMR* **2001**, *21*, 349–359.
- [8] K. J. Yong, T. M. Vaid, P. J. Shilling, F.-J. Wu, L. M. Williams, M. Deluigi, A. Plückthun, R. A. D. Bathgate, P. R. Gooley, D. J. Scott, *ACS Chem. Biol.* **2018**, *13*, 1090–1102.
- [9] S. Barelier, D. Linard, J. Pons, A. Clippe, B. Knoops, J.-M. Lancelin, I. Krimm, *PLoS One* **2010**, *5*, e9744.
- [10] S. Ignot, C. Raingeval, E. Cecon, M. Pučić-Baković, G. Lauc, O. Cala, M. Baranowski, J. Perez, R. Jockers, I. Krimm, A. Jawhari, *Sci. Rep.* **2018**, *8*, 8142.
- [11] M. F. Mesleh, W. A. Shirley, C. E. Heise, N. Ling, R. A. Maki, R. P. Laura, *J. Biol. Chem.* **2007**, *282*, 6338–6346.
- [12] P. M. Nieto, *Front. Mol. Biosci.* **2018**, *5*, 33.
- [13] C. A. Softley, M. J. Bostock, G. M. Popowicz, M. Sattler, *J. Biomol. NMR* **2020**, *74*, 287–309.
- [14] M. John, G. Pintacuda, A. Y. Park, N. E. Dixon, G. Otting, *J. Am. Chem. Soc.* **2006**, *128*, 12910–6.
- [15] T. Zhuang, H.-S. Lee, B. Imperiali, J. H. Prestegard, *Protein Sci.* **2008**, *17*, 1220–1231.
- [16] J. Y. Guan, P. H. Keizers, W. M. Liu, F. Lohr, S. P. Skinner, E. A. Heeneman, H. Schwalbe, M. Ubbink, G. Siegal, *J. Am. Chem. Soc.* **2013**, *135*, 5859–68.
- [17] G. Kuenze, S. Köhling, A. Vogel, J. Rademann, D. Huster, *J. Biol. Chem.* **2016**, *291*, 3100–3113.
- [18] W. N. Chen, C. Nitsche, K. B. Pilla, B. Graham, T. Huber, C. D. Klein, G. Otting, *J. Am. Chem. Soc.* **2016**, *138*, 4539–46.
- [19] K. Zimmermann, D. Joss, T. Müntener, E. S. Nogueira, M. Schäfer, L. Knör, F. W. Monnard, D. Häussinger, *Chem. Sci.* **2019**, *10*, 5064–5072.
- [20] U. Brath, S. I. Swamy, A. X. Veiga, C.-C. Tung, F. Van Petegem, M. Erdélyi, *J. Am. Chem. Soc.* **2015**, *137*, 11391–11398.
- [21] Á. Canales, Á. Mallagaray, M. Á. Berbís, A. Navarro-Vázquez, G. Domínguez, F. J. Cañada, S. André, H.-J. Gabius, J. Pérez-Castells, J. Jiménez-Barbero, *J. Am. Chem. Soc.* **2014**, *136*, 8011–8017.
- [22] S. Köhling, G. Kuenze, K. Lemmnitzer, M. Bermudez, G. Wolber, J. Schiller, D. Huster, J. Rademann, *Chemistry* **2016**, *22*, 5563–5574.
- [23] C. Hartlmüller, J. C. Günther, A. C. Wolter, J. Wöhner, M. Sattler, T. Madl, *Sci. Rep.* **2017**, *7*, 5393.
- [24] K.-Y. Lee, Z. Fang, M. Enomoto, G. Gasmi-Seabrook, L. Zheng, S. Koide, M. Ikura, C. B. Marshall, *Angew. Chem. Int. Ed.* **2020**, *59*, 11037–11045.
- [25] C. Hartlmüller, C. Göbl, T. Madl, *Angew. Chem. Int. Ed.* **2016**, *55*, 11970–11974.
- [26] Y. Wang, C. D. Schwieters, N. Tjandra, *J. Magn. Reson.* **2012**, *221*, 76–84.
- [27] C. Hartlmüller, E. Spreitzer, C. Göbl, F. Falsone, T. Madl, *J. Biomol. NMR* **2019**, *73*, 305–317.
- [28] S. Arumugam, C. L. Hemme, N. Yoshida, K. Suzuki, H. Nagase, M. Berjanskii, B. Wu, S. R. Van Doren, *Biochemistry* **1998**, *37*, 9650–9657.
- [29] T. Madl, T. Güttler, D. Görlich, M. Sattler, *Angew. Chem. Int. Ed.* **2011**, *50*, 3993–3997.
- [30] J. H. Tomlinson, G. S. Thompson, A. P. Kalverda, A. Zhuravleva, A. J. O'Neill, *Sci. Rep.* **2016**, *6*, 19524.
- [31] B. Yu, C. C. Pletka, B. M. Pettitt, J. Iwahara, *Proc. Natl. Acad. Sci. USA* **2021**, *118*, DOI 10.1073/pnas.2104020118.
- [32] B. Yu, C. C. Pletka, J. Iwahara, *Proc. Natl. Acad. Sci. USA* **2021**, *118*, DOI 10.1073/pnas.2015879118.
- [33] B. Yu, X. Wang, J. Iwahara, *J. Phys. Chem. Lett.* **2022**, *13*, 10025–10029.
- [34] P. Kukić, J. E. Nielsen, *Future Med. Chem.* **2010**, *2*, 647–666.
- [35] R. Alsallaq, H.-X. Zhou, *Proteins* **2008**, *71*, 320–335.
- [36] A. Voet, F. Berenger, K. Y. J. Zhang, *PLoS One* **2013**, *8*, e75762.
- [37] M. R. Bauer, M. D. Mackey, *J. Med. Chem.* **2019**, *62*, 3036–3050.
- [38] K. Rajarathnam, B. D. Sykes, C. M. Kay, B. Dewald, T. Geiser, M. Baggolini, I. Clark-Lewis, *Science* **1994**, *264*, 90–92.
- [39] S. T. Das, L. Rajagopalan, A. Guerrero-Plata, J. Sai, A. Richmond, R. P. Garofalo, K. Rajarathnam, *PLoS One* **2010**, *5*, e11754.
- [40] A. Pichert, D. Schlorke, S. Franz, J. Arnhold, *Biomatter* **2012**, *2*, 142–148.
- [41] D. Spillmann, D. Witt, U. Lindahl, *J. Biol. Chem.* **1998**, *273*, 15487–15493.
- [42] G. S. V. Kuschert, A. J. Hoogewerf, A. E. I. Proudfoot, C. Chung, R. M. Cooke, R. E. Hubbard, T. N. C. Wells, P. N. Sanderson, *Biochemistry* **1998**, *37*, 11193–11201.
- [43] B. Goger, Y. Halden, A. Rek, R. Mösl, D. Pye, J. Gallagher, A. J. Kungl, *Biochemistry* **2002**, *41*, 1640–1646.
- [44] A. Pichert, S. A. Samsonov, S. Theisgen, L. Thomas, L. Baumann, J. Schiller, A. G. Beck-Sickinger, D. Huster, M. T. Pisabarro, *Glycobiology* **2012**, *22*, 134–145.
- [45] K. Nordsieck, A. Pichert, S. A. Samsonov, L. Thomas, C. Berger, M. T. Pisabarro, D. Huster, A. G. Beck-Sickinger, *ChemBioChem* **2012**, *13*, 2558–2566.
- [46] K. Möbius, K. Nordsieck, A. Pichert, S. A. Samsonov, L. Thomas, J. Schiller, S. Kalkhof, M. Teresa Pisabarro, A. G. Beck-Sickinger, D. Huster, *Glycobiology* **2013**, *23*, 1260–1269.
- [47] T. Hofmann, S. A. Samsonov, A. Pichert, K. Lemmnitzer, J. Schiller, D. Huster, M. T. Pisabarro, M. von Bergen, S. Kalkhof, *Methods* **2015**, *89*, 45–53.
- [48] S. Maignan, J.-P. Guilloteau, N. Fromage, B. Arnoux, J. Becquart, A. Ducruix, *Science* **1995**, *268*, 291–293.
- [49] P. Chardin, D. Cussac, S. Maignan, A. Ducruix, *FEBS Lett.* **1995**, *369*, 47–51.
- [50] M. Rozakis-Adcock, R. Fernley, J. Wade, T. Pawson, D. Bowtell, *Nature* **1993**, *363*, 83–85.
- [51] J. R. Molina, A. A. Adjei, *J. Thorac. Oncol.* **2006**, *1*, 7–9.
- [52] Z. Songyang, S. E. Shoelson, J. McGlade, P. Olivier, T. Pawson, X. R. Bustelo, M. Barbacid, H. Sabe, H. Hanafusa, T. Yi, R. Ren, D. Baltimore, S. Ratnofsky, R. A. Feldman, L. C. Cantley, *Mol. Cell. Biol.* **1994**, *14*, 2777–2785.
- [53] H. Gram, R. Schmitz, J. F. Zuber, G. Baumann, *Eur. J. Biochem.* **1997**, *246*, 633–637.
- [54] G. M. Clore, E. Appella, M. Yamada, K. Matsushima, A. M. Gronenborn, *Biochemistry* **1990**, *29*, 1689–1696.
- [55] N. A. Baker, D. Sept, S. Joseph, M. J. Holst, J. A. McCammon, *Proc. Natl. Acad. Sci. USA* **2001**, *98*, 10037–10041.
- [56] E. Jurrus, D. Engel, K. Star, K. Monson, J. Brandi, L. E. Felberg, D. H. Brookes, L. Wilson, J. Chen, K. Liles, M. Chun, P. Li, D. W. Gohara, T. Dolinsky, R. Konecny, D. R. Koes, J. E. Nielsen, T. Head-Gordon, W. Geng, R. Krasny, G.-W. Wei, M. J. Holst, J. A. McCammon, N. A. Baker, *Protein Sci.* **2018**, *27*, 112–128.
- [57] P. R. B. Joseph, P. D. Mosier, U. R. Desai, K. Rajarathnam, *Biochem. J.* **2015**, *472*, 121–133.
- [58] K. Nordsieck, L. Baumann, V. Hintze, M. T. Pisabarro, M. Schnabelrauch, A. G. Beck-Sickinger, S. A. Samsonov, *Biopolymers* **2018**, *109*, e23103.
- [59] P. Nioche, W. Q. Liu, I. Broutin, F. Charbonnier, M. T. Latreille, M. Vidal, B. Roques, C. Garbay, A. Ducruix, *J. Mol. Biol.* **2002**, *315*, 1167–77.
- [60] S. Yuzawa, K. Ogura, H. Hatanaka, K. Miura, F. Inagaki, *J. Biomol. NMR* **2003**, *27*, 185–186.
- [61] K. Sanches, I. P. Caruso, F. C. L. Almeida, F. A. Melo, *Biomol NMR Assign* **2019**, *13*, 295–298.
- [62] K. Ogura, T. Shiga, M. Yokochi, S. Yuzawa, T. R. Burke Jr., F. Inagaki, *J. Biomol. NMR* **2008**, *42*, 197–207.
- [63] Y. Okuno, C. D. Schwieters, Z. Yang, G. M. Clore, *J. Am. Chem. Soc.* **2022**, *144*, 21371–21388.
- [64] S. Mori, C. Abeygunawardana, M. O. Johnson, P. C. M. Vanzijl, *J. Magn. Reson. Ser. B* **1995**, *108*, 94–98.
- [65] J. Iwahara, C. Tang, G. Marius Clore, *J. Magn. Reson.* **2007**, *184*, 185–195.
- [66] W. Lee, M. Tonelli, J. L. Markley, *Bioinformatics* **2015**, *31*, 1325–1327.
- [67] D. A. Case, K. Belfon, I. Y. Ben-Shalom, S. R. Brozell, D. S. Cerutti, T. E. Cheatham III, **2020, AMBER 2020**, University of California, San Francisco.
- [68] B. Mulloy, M. J. Forster, C. Jones, D. B. Davies, *Biochem. J.* **1993**, *293*(Pt 3), 849–858.
- [69] A. Almond, P. L. DeAngelis, C. D. Blundell, *J. Mol. Biol.* **2006**, *358*, 1256–1269.
- [70] G. M. Morris, D. S. Goodsell, R. S. Halliday, R. Huey, W. E. Hart, R. K. Belew, A. J. Olson, *J. Comput. Chem.* **1998**, *19*, 1639–1662.
- [71] M. Ester, H. P. Kriegel, J. Sander, X. Xiaowei, *Proceedings of 2nd International Conference on Knowledge Discovery and Data Mining (KDD) 1996*, *KDD-96*, 226–231.

- [72] H. Nguyen, J. Maier, H. Huang, V. Perrone, C. Simmerling, *J. Am. Chem. Soc.* **2014**, *136*, 13959–13962.
- [73] K. N. Kirschner, A. B. Yongye, S. M. Tschampel, J. González-Outeiriño, C. R. Daniels, B. L. Foley, R. J. Woods, *J. Comput. Chem.* **2008**, *29*, 622–655.
- [74] T. Steinbrecher, J. Latzer, D. A. Case, *J. Chem. Theory Comput.* **2012**, *8*, 4405–4412.
- [75] W. Humphrey, A. Dalke, K. Schulten, *J. Mol. Graphics* **1996**, *14*, 33–38.
- [76] D. R. Roe, T. E. Cheatham 3rd, *J. Chem. Theory Comput.* **2013**, *9*, 3084–95.
- [77] A. Onufriev, D. Bashford, D. A. Case, *J. Phys. Chem. B* **2000**, *104*, 3712–3720.
- [78] N. M. O’Boyle, M. Banck, C. A. James, C. Morley, T. Vandermeersch, G. R. Hutchison, *J. Cheminform* **2011**, *3*, 33.

Manuscript received: October 27, 2023

Accepted manuscript online: November 29, 2023

Version of record online: February 13, 2024